Modeling lithospheric thickness along the conjugate South Atlantic passive margins implies asymmetric rift initiation

Peter Haas[1], R. Dietmar Müller[2], Jörg Ebbing[1], Nils-Peter Finger[3,4] and Mikhail K. Kaban[3,5]

[1]Institute of Geosciences, Kiel University, Kiel, Germany

[2]Earthbyte Group, School of Geosciences, The University of Sydney, Sydney, Australia

[3]GFZ Research Centre for Geosciences, Potsdam, Germany

[4]Free University of Berlin, Berlin, Germany

[5]Schmidt Institute of Physics of the Earth, Moscow, Russia

Corresponding author: Peter Haas (peter.haas@ifg.uni-kiel.de)

Key Points:

- A simple thermal LAB model for the South Atlantic passive margins has been developed
- The LAB model shows highly variable lithospheric thickness that reflects different rifting stages of the South Atlantic
- The difference of LAB depths for conjugate margin pairs correlates with asymmetry in margin width, implying asymmetric lithospheric thinning

Abstract

The lithospheric architecture of passive margins is crucial for understanding the tectonic processes that caused the break-up of Gondwana. We highlight the evolution of the South Atlantic passive margins by a simple thermal lithosphere-asthenosphere-boundary (LAB) model based on rifting time, crustal thickness, and stretching factors. We simulate the different rifting stages that caused the opening of the South Atlantic Ocean and pick the LAB as the T=1330 °C isotherm, which is calculated by 1D advection and diffusion. In a synthetic example, we demonstrate that the initial crustal thickness has the largest effect on the thermal LAB. For the South American passive margin, our modeled LAB shows a deep and smooth structure between 110-150 km depth at equatorial latitudes and a more variable LAB between 50-200 km along the southern part. This division reflects different stages of the South Atlantic opening: initial opening of the southern South Atlantic causing substantial lithospheric thinning, followed by rather oblique opening of the equatorial South Atlantic accompanied by severe thinning. The modeled LAB reflects a high variability associated with tectonic features on a small scale. Comparing the LAB of the conjugate South American and African passive margins in a Gondwana framework reveals a variable lithospheric architecture for the southern conjugate margins. Along selected conjugate margin segments stark differences up to 80 km of the LAB depths correlate with strong gradients in margin width. This mutual asymmetry suggests highly asymmetric melting and lithospheric thinning prior to rifting.

Plain Language Summary

Passive margins mark the transition zone from a continent to the ocean without being an active boundary of tectonic plates. They are typical for all continents on the globe. In the South Atlantic, the passive margins are located adjacent to the eastern coastline of South America and the western coastline of Africa. Studying the architecture of passive margins is essential for understanding plate tectonic history of the earth because they define how the continents once belonged together and how they broke apart. Passive margin segments on opposite sides of an ocean form so called conjugate margin pairs. Most geophysical studies of passive margins focus on the near-surface architecture. However, their deeper extension to the base of the rigid shell of the earth, known as lithospheric thickness, is to a large extent unknown. Based on a simple temperature model we find that the lithospheric thickness is highly variable and shows structural variations along the South Atlantic passive margins. These differences are associated with the extension of conjugate margin pairs: where one margin is narrower than the conjugate, its lithospheric thickness is greater. This asymmetry indicates that the geodynamic processes, causing the break-up of the two continents, must have been asymmetric as well.

1 Introduction

The architecture and evolution of passive margins have been extensively studied over the last decades (e.g., Duretz et al., 2016; Geoffroy, 2005; Lister et al., 1986; Reston, 2009). For a long time, this was predominantly motivated by hydrocarbon exploration because numerous oil and gas reservoirs are connected to passive margin formation. Nowadays, passive margins become the focus of attention for sequestering carbon dioxide (e.g., Ringrose and Meckel, 2019), as well as for estimating the global carbon dioxide budget over deep time (e.g., Brune et al., 2017).

The McKenzie model of rifting is a widely accepted model that explains thinning of the continental lithosphere and subsequent stretching in pure-shear mode associated with tectonic subsidence (McKenzie, 1978). Jarvis and McKenzie (1980) introduced a time-dependent

analytical model that relates variations in heat flow and subsidence history to the rate of extension. The formation of non-volcanic passive margins is the endmember of the McKenzie rifting model with passive upwelling of buoyant sublithospheric mantle material, driven by far field extension forces (Geoffroy, 2005; Sengör and Burke, 1978).

In many places, volcanic passive margins have been interpreted as the result of active upwelling of a mantle plume, associated with a thick crust due to magmatic underplating and the formation of Seaward Dipping Reflectors (SDR; e.g., Geoffroy, 2005; Mutter et al., 1982). The occurrence of volcanic rifted margins does not necessarily require a pronounced thermal anomaly in the mantle related to a plume (e.g., Bown and White, 1995), but can be explained with transient small-scale mantle convection underneath the lithosphere (Nielsen, 2002; Simon et al., 2009) or plume-rift interaction (Morgan et al., 2020).

The crustal architecture of passive margins shows a high diversity that cannot be characterized only in terms of magmatic budget (e.g., Tugend et al., 2018). One important observation is asymmetry of opposed margins, which requires other mechanisms than pure shear (Lister et al., 1986). A proposed mechanism is detachment faulting along low-angle normal faults, which cut through the entire lithosphere (Lister et al., 1986). This concept is based on simple shear (Wernicke, 1981). Brune et al. (2014) showed that margin asymmetry is caused by rift migration of only upper crustal faults, associated with a large melt transfer between two rift sides. Tugend et al. (2018) propose that timing of decompression melting may be more important than estimates of the magmatic budget of passive margins to understand their evolution and variability.

All rifting models have in common that the initial lithospheric thickness is thinned prior to rifting, followed by subsidence and cooling of the lithosphere. The concept of half-space cooling predicts lithospheric thickening with time during the first ~80 million years after crustal accretion at a mid-ocean-ridge (e.g., Turcotte and Schubert, 2018). However, at passive margins this concept fails as the oceanic crust is older than 80 Ma in many places and the relation of passive and active upwelling of mantle material is not known. Due to this ambiguity, the amount of lithospheric thinning prior to margin formation is also often unknown.

In this study, we focus on the formation and lithospheric thickness of the South Atlantic passive margins. Their architecture cannot be explained by uniform rifting models only and shows a wide range of volcanic and non-volcanic passive margin types. In the Late Jurassic, rifting started and caused the disintegration of Western Gondwana, leading to the opening of the southern South Atlantic (e.g., Rabinowitz and LaBrecque, 1979). In the Late Aptian/Early Albian, the equatorial part of the South Atlantic opened (Moulin et al., 2010), characterized by a higher degree of oblique rifting (Brune et al., 2018). The equatorial opening of the South Atlantic was dominated by far field forces (e.g., Heine et al., 2013; Moulin et al., 2010).

To what extent the Tristan Hotspot, which formed the Parana-Etendeka flood basalts (Granot and Dyment, 2015; Renne et al., 1992), contributed to the initial break-up is still discussed. Combined seismic imaging and potential field data analysis for the central and southern segments of the South Atlantic suggests that the Tristan Hotspot sourced the magmatism volume but might not necessarily have altered the process of rifted margin formation (Blaich et al., 2011). Comparison between Large Igneous Provinces (LIP) and break-up age shows that rifting occurred before LIP emplacement. This indicates that rifting might have been initiated by tectonic forces and the Tristan plume only guides the mantle material towards the thinned lithosphere (Buiter and Torsvik, 2014). Morgan et al. (2020) propose that along-rift flow of

plume material causes the formation of volcanic passive margins, associated with thinning of the initial lithosphere.

In recent years, several global and regional lithospheric thickness models have been published that cover the South Atlantic passive margins. Global models are, for example, derived from surface-wave dispersion maps (Pasyanos et al., 2014), conversion of seismic tomography to thermal LAB (Steinberger and Becker, 2018) or multi-probabilistic joint inversion (Afonso et al., 2019). The global LAB models have a wide depth range, partly depending on the data sets and regularizations used in establishing the models. Due to the narrow and elongated margin geometry, many of these global models are not capable of mapping the LAB in this region. For example, Finger et al. (2021) present a regional model for the South American continent based on combined density, thermal, and compositional modeling, which can be converted to a LAB model. However, the thermal field, which can be converted to LAB depths, does not adequately represent the passive margins as their modeling approach focusses on the continental platforms.

In this paper, we predict a thermal LAB depth of the stretched region along the passive margins of the South Atlantic. We first introduce our method for the South American passive margin. The thermal LAB depth is derived from three input parameters: stretching factors, rifting time, and crustal thickness. We calculate the stretching factors by accounting for crustal thickness gradients across the deforming region. Together with rifting time and published crustal thickness models, we then calculate a thermal model of the extended lithosphere. The LAB depth is defined by extrapolating the linear geotherm from the crust throughout the lithosphere after rifting occurred. Next, we discuss the evolution of the thermal LAB for the conjugate South Atlantic passive margins in a Gondwana framework using GPlates software (Müller et al., 2018). We further evaluate differences between conjugate margin basins by correlating the predicted LAB depth with margin width.

2 Methods

We calculate lithospheric thickness as a function of rifting time, crustal thickness, and stretching factor. For that, we use the python code *RiftSubsidence* based on software that was originally designed to calculate theoretical subsidence curves for rifting scenarios in 1D (White et al., pers. com.). In *RiftSubsidence*, the subsidence is calculated based on the amount and timing of pure shear lithospheric extension, as well as on the thermal and density structure of the lithosphere.

In this approach, the lithospheric thickness is derived from the thermal structure after the lithosphere has been stretched. The temperature of the model is calculated by 1D advection and diffusion using finite differences. The top of the model is defined at sea level, while the base of the model is defined as the LAB. At these boundaries, the temperature is fixed throughout the entire rifting period.

Prior to lithospheric stretching the LAB depth z_{LAB} and LAB temperature T_{LAB} must be defined. z_{LAB} is balanced isostatically against a reference Mid-Ocean-Ridge (MOR). Figure 1 shows the isostatic model of the reference MOR on the left and passive margin on the right. Assuming that the thickness of the mantle lithosphere h_m is the only unknown parameter, the isostatic equation can be defined as:

$$h_m = \frac{\rho_w h_w + \rho_c(h_{c0} - h_c) + \rho_a(h_c - h_w - h_{c,ref})}{(\rho_m - \rho_a)} \qquad (1)$$

The assumed values of density and thickness of each layer are listed in Table 1. The crustal thickness varies spatially for the passive margin. Accordingly, the initial LAB depth z_{LAB} is individual for each point and is defined as: $z_{LAB} = h_c + h_m$. For crustal density, we calculate the

average value over the entire deformable region (see Table 1). The value of $\rho_c = 2.809$ g/cm³ is obtained by balancing isostatically thicknesses and densities of crystalline crust and sediments of the crustal model of Finger et al. (2021). Thus, it represents a mean value of the entire crust.

Variable	Name	Value
ρ_w	Density of sea water	1.03 g/cm³
ρ_c	Density of crust	2.809 g/cm³ [1]
ρ_m	Density of lithospheric mantle	Unknown
ρ_a	Density of asthenosphere	3.3 g/cm³ [3]
h_w	Height of sea water	2.5 km [2]
$h_{c,ref}$	Thickness of crust at MOR	7 km [2]
h_c	Thickness of crust	Variable [1]
h_m	Thickness of lithospheric mantle	Unknown

Table 1. Layers of isostatic model at passive margin with respective densities. [1]Thickness and density of the crust are taken from Finger et al. (2021). [2]Thicknesses of MOR reference column are taken from Afonso et al. (2019). [3]Density of asthenosphere taken from Zoback and Mooney (2010).

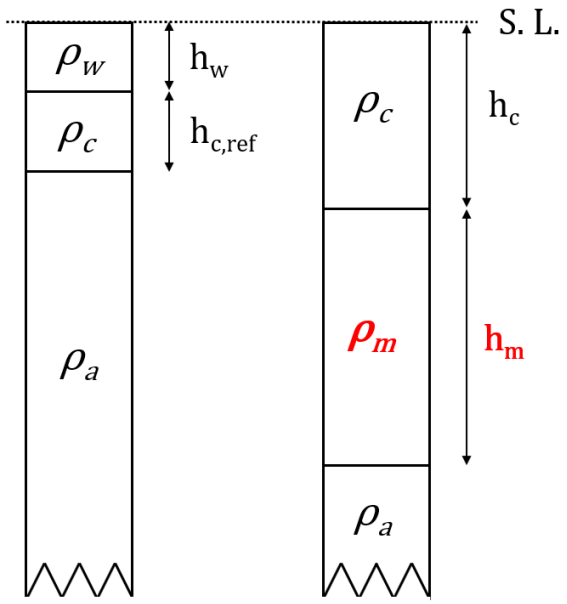

Figure 1. Isostatic balance of MOR (left) and passive margin (right). Mantle density and thickness of mantle lithosphere are the unknown parameters. Full names of the parameters are given in Table 1.

The isostatic balance in Eq. 1 assumes a constant mantle density. As the South American passive margin is bounded by different continental and oceanic tectonic regimes, its mantle density is heterogeneous. Estimates from global and regional inversions indicate varying mantle densities along the South American passive margin (e.g., Afonso et al., 2019; Finger et al., 2021). Therefore, the mantle density is the second unknown parameter of the isostatic column.

Prior to rifting the thermal state of the lithosphere can be regarded as purely conductive with a linear geotherm. Assuming a constant linear geotherm for the entire lithosphere (blue lines in Figure 2), we calculate the mantle density and thickness of the mantle lithosphere in an iterative scheme:

1. Select a starting value of $h_{m,0}$
2. As the geotherm is linear throughout the lithosphere, the mantle temperature T_m can be directly derived from T_{LAB} and the temperature at the Moho T_{Moho}:

$$T_m = \frac{T_{LAB} + T_{Moho}}{2} \quad (2)$$

T_{Moho} can be substituted by the quotient of crustal and lithospheric thickness:

$$T_m = \frac{T_{LAB}\left(1 + \frac{h_c}{h_c + h_{m,i}}\right)}{2} \quad (3)$$

With $h_{m,i}$ = thickness of mantle lithosphere at iteration step *i*.

3. Assume mantle density as a function of temperature, based on volumetric coefficient of thermal expansion α (e.g., Turcotte and Schubert 2018):

$$d\rho = -\rho\alpha dT \quad (4)$$

Solve the differential:

$$\rho_a - \rho_{m,i} = -\rho_{m,i}\alpha(T_{LAB} - T_m) \quad (5)$$

Solve Eq. 5 for mantle density:

$$\rho_{m,i} = \frac{\rho_a}{1 - \alpha(T_{LAB} - T_m)} \quad (6)$$

With $\rho_{m,i}$ =mantle density at the iteration step *i* and α=thermal expansivity coefficient [1/K]

4. Update h_m based on Eq. 1 and mantle density of Eq. 6.
5. Repeat Step 2-4

The process is iterated until the density change reaches the threshold $\|\rho_{m,i+1} - \rho_{m,i}\| < 0.001$ g/cm³. For T_{LAB} and α we choose standard values of T_{LAB}*=1333 °C* and α*=3.28*10^{-5} 1/K* (e.g., Jarvis and McKenzie, 1980; Parsons and Sclater, 1977). More specific values of α for oceanic lithosphere exist (*α=3.45)*, which are derived from mineral physics (Afonso et al., 2005). However, the effect on the modeled LAB is only minor.

z_{LAB} represents the depth of the LAB prior to rifting. If the lithosphere is not stretched, a linear geotherm for the entire lithosphere can be assumed. However, rifting causes lithospheric extension with subsequent non-linear displacement of the geotherm. After extension ceases, the lithosphere cools and the geotherm relaxes back to the linear state at infinite time. Depending on initiation and end of rifting and the amount of stretching, the geotherm will deviate from its initial linear state (Figure 2). If we assume that conductive heat transport in the crust is the

dominant heat source and that thermal expansion is constant both for the crust and lithosphere, we can extrapolate the geotherm of the crust throughout the mantle lithosphere. As a result, z_{LAB} is shifted upward (Figure 2). The difference between $z_{LAB,init}$ based on the isostatic model and $z_{LAB,rifted}$ based on the extrapolated crustal geotherm, is defined as Δz_{LAB}.

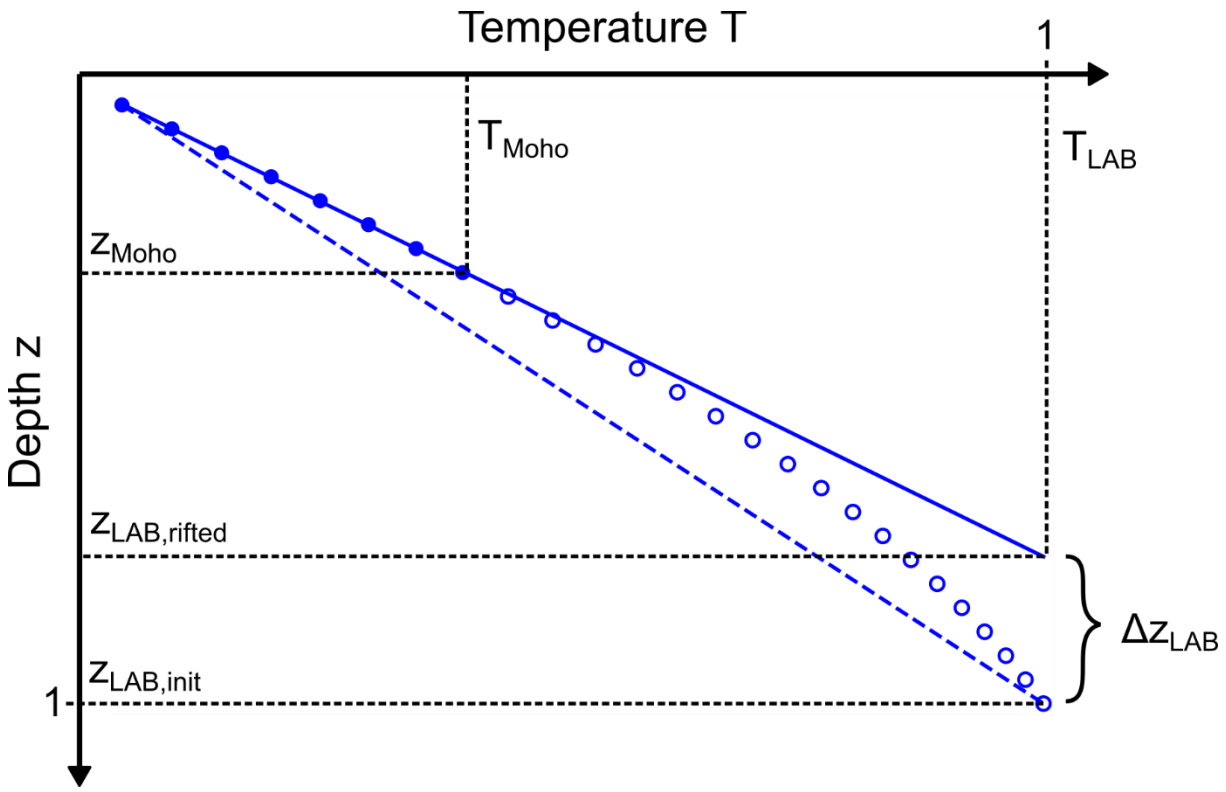

Figure 2. Geotherms and the LABs. Dashed line: Initial geotherm before rifting, circles: uplifted geotherm after rifting and cooling, solid blue line: extrapolated linear geotherm based on thermal structure of crust (filled circles). The depth at which the extrapolated geotherm reaches T_{LAB} provides an approximate estimate of z_{LAB}.

The amount of non-linearity of the distorted geotherm in Figure 2 depends on the elapsed time and on the amount of stretching. Based on the concepts described by McKenzie (1978), we define the stretching factor as the thickness of unthinned crust divided by thinned crust:

$$ß = \frac{h_i}{h_s} \quad (7)$$

h_i defines the initial crustal thickness, whereas h_s is the crustal thickness after stretching. Müller et al. (2019) used this approach to derive stretching factors globally for all deforming regions. However, their values are calculated based on uniform stretching and do not consider crustal thickness gradients. We derive new stretching factors for the South American passive margin, by selecting an updated crustal thickness model of South America by Finger et al. (2021), which is based on available seismic determinations.

The Continent-Ocean-Boundary (COB) can be divided in an inner part, defined as the landward limit of stretched continental crust, and an outer part, defined as the oceanward limit of stretched continental crust (Müller et al., 2019). The area between the inner and outer COB is defined as the deforming region and represents the thinned crust h_s (see Figure 3). In the following, we will

240 treat the term ‘deforming region’ as ‘passive margin’. To obtain the unthinned crust h_i, the inner
241 margin of the COB is extended 500 km towards the continent. Figure 3a shows the crustal
242 thickness of Finger et al. (2021), where the South American passive margin is defined by its
243 inner and outer COB. For the equatorial and southern margin different rifting stages are assumed.
244 We define five different segments of extended COB, based on adjacent onshore crustal thickness
245 and surface geology. For each segment, we calculate the mean value of crustal thickness, which
246 represents unthinned crust h_i (Figure 3b). Table 2 lists the average values of the different
247 segments. Note that the average crustal thickness of units 2-5 is almost identical. Figure 3c
248 shows the resulting stretching factor.
249

Segment	Geology	Crustal Thickness [km]
1	Colorado Basin (offshore)	29,9
2	Parana Basin	38,2
3	Sao Francisco	38,8
4	Amazonia South	38,6
5	Amazonia North	37,5

250 **Table 2**. Average crustal thickness values for the different geological segments shown in
251 Figure 3b.
252

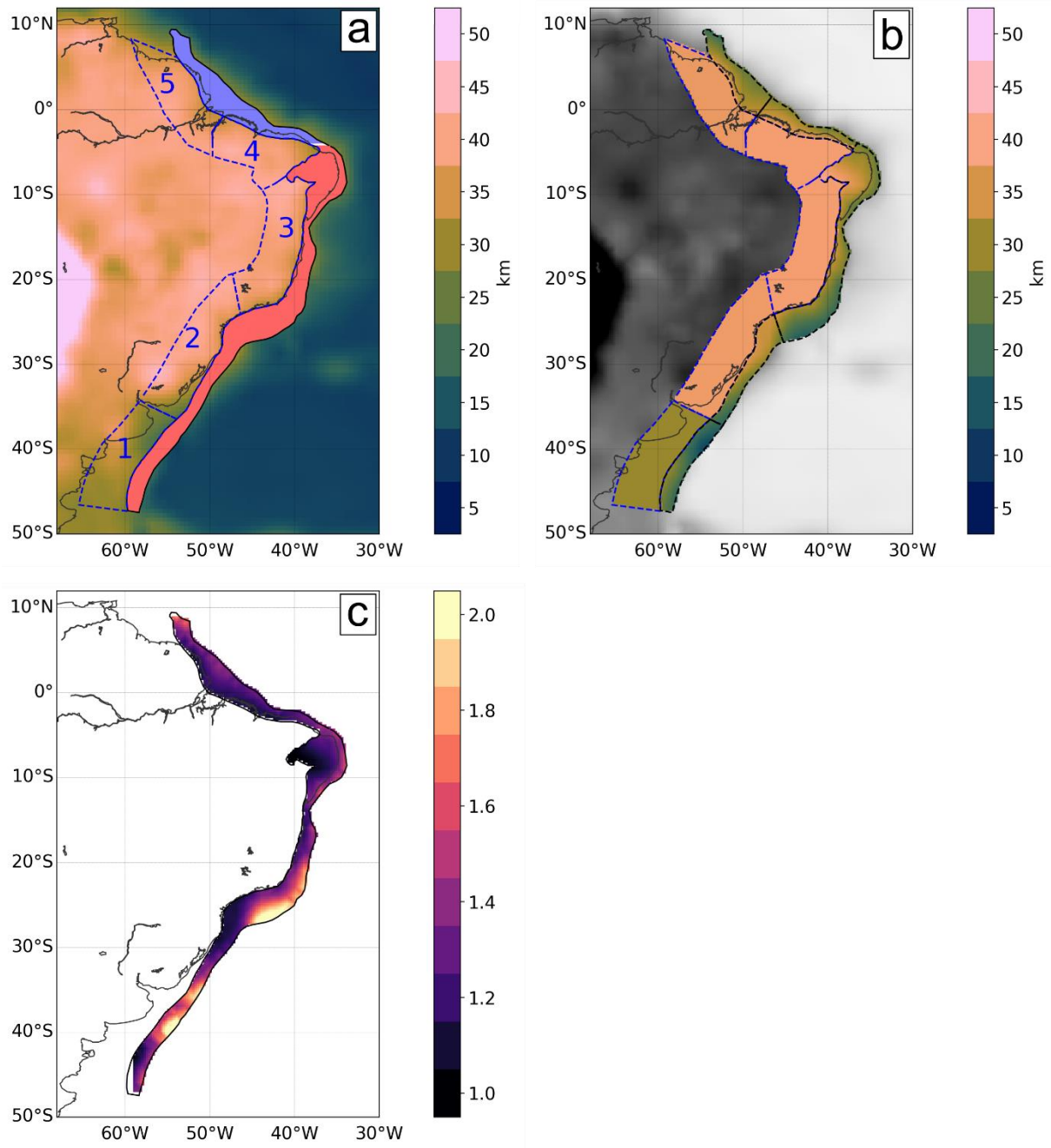

Figure 3. Crustal thickness to calculate stretching factors. **a**: Crustal thickness model of Finger et al. (2021). Masked area: Geometry of the South American passive margin. The coral polygon corresponds to the early opening of the Atlantic from 141-120 Ma, the blue polygon to the later stage from 121-107 Ma (rifting time taken from the GPlates data base, as published in Müller et al., 2019). Blue dashed contours and numbers represent different segments of crustal thickness, extended 500 km towards the inner continent. **b**: Crustal thickness values for deformable region and inner extension area. Values for inner area are averaged. **c**: Stretching factors of deforming region of passive margin.

3 Synthetic example – Varying input parameters of *RiftSubsidence*

Originally, *RiftSubsidence* was designed to calculate theoretical subsidence curves based on the input parameters rifting time, stretching factor, and crustal thickness (White et al., pers. com.). Within the following synthetic example, we show the effect of each parameter on the resulting lithospheric thickness after rifting.

First, we select default values of the initial parameters. For rifting time t_{rift} we choose 130-50 Ma, stretching factor $ß = 2$, crustal thickness $h_c = 30$ km. Each parameter is varied in a certain range, while the other parameters are fixed at the respective default values. Densities and thicknesses of the isostatic reference model are taken from Table 1. Here, we assume a constant mantle density of $\rho_m = 3.35$ g/cm³. According to Eq. 1, the only unknown parameter is now h_m. In another synthetic example, we vary the densities of the reference isostatic column and investigate to which extent this contributes to the LAB depth after rifting (supporting information S1).

We investigate two different scenarios of t_{rift}: first, we set the initiation of rifting at 130 Ma and vary the end from 120 to 0 Ma. Second, we set a constant duration of rifting of 80 Ma and start at 200 Ma. Figure 4 shows the end time of rifting versus the LAB depth after rifting $z_{LAB,rifted}$. For constant time of rifting initiation at 130 Ma $z_{LAB,rifted}$ decreases towards the present time. The same trend can be observed for a constant duration of rifting, but $z_{LAB,rifted}$ is even shallower than before. $z_{LAB,rifted}$ is progressively decreasing towards the present day. The shorter the rifting time, the less time the lithosphere has to cool down, resulting in an uplifted geotherm and a stronger deviation from the initial isostatic LAB $z_{LAB,init}$. Comparing both scenarios, the advection rate is the same only if the period of extension and the stretching factor are the same. $z_{LAB,rifted}$ becomes shallower for the model with constant duration of rifting because the extension has occurred until more recent times (For example, 130-0 Ma for the red curve vs. 80-0 Ma for the blue curve).

By varying the stretching factor $ß$ between 1-3 and taking the default values of the other parameters, we observe an almost linear shallowing of $z_{LAB,rifted}$ towards higher stretching factor (Figure 5). The difference of ~20 km between $z_{LAB,rifted}$ and $z_{LAB,init}$ is of the same magnitude as with the variable rifting time in Figure 4. Figure 5 also shows the LAB depth after varying the initial crustal thickness between 20-40 km. Note that in this case $z_{LAB,init}$ is not constant. Increasing the Moho depth causes increasing the LAB depth. Isostasy shows that the mass deficit of a deeper Moho is compensated by a thicker mantle lithosphere (right column of Figure 1). This trend is not linear because the crustal thickness h_c controls two coefficients ρ_c and ρ_a in Eq. 1. At the of Moho depth ~26 km and LAB depth of ~60 km, $z_{LAB,rifted}$ starts to deviate from $z_{LAB,init}$. The effect becomes stronger with increasing the Moho depth. Here, the effect of rifting and stretching becomes significant. For this configuration, a ratio of the Moho and LAB depths of 0.43 is the threshold for significant difference between $z_{LAB,init}$ and $z_{LAB,rifted}$.

This synthetic example demonstrates that the initial crustal thickness has the strongest effect on $z_{LAB,rifted}$. In the supporting information we show how $z_{LAB,rifted}$ varies for spatially variable crustal thickness, using two recently published crustal thickness models of South America (Finger et al., 2021; Haas et al., 2020).

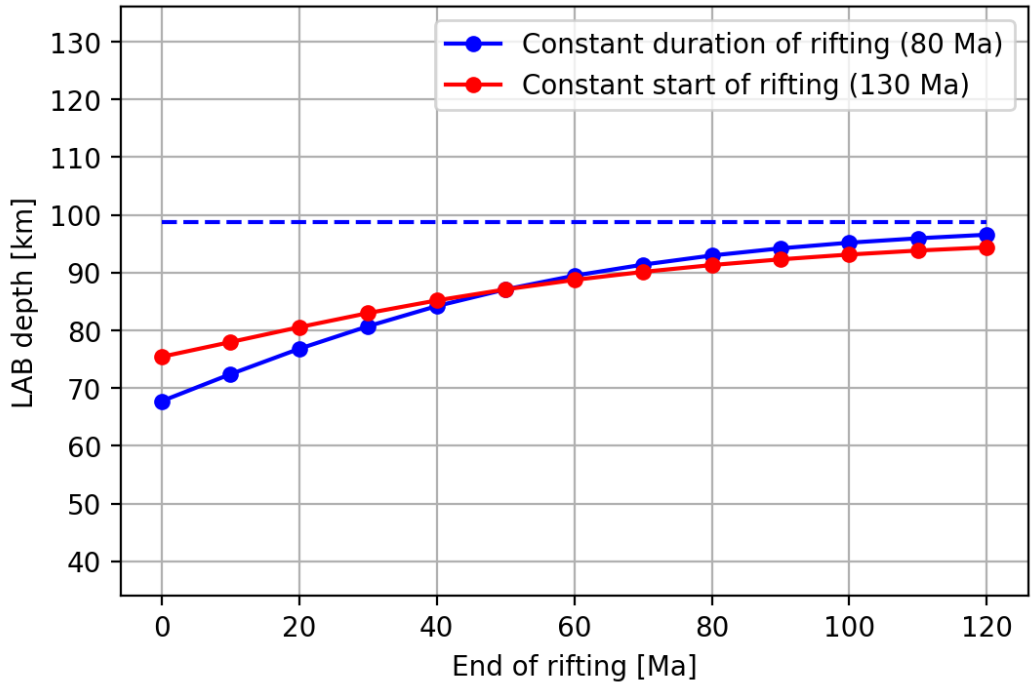

Figure 4. Rifting time vs. LAB depth for different initiation time and duration of rifting. The red curve shows the $z_{LAB,rifted}$ for constant start of rifting at 130 Ma with variable end between 120 to 0 Ma. The blue curve indicates $z_{LAB,rifted}$ for constant duration of rifting of 80 Ma with variable onset of rifting. The first red dot on the right side cuts the x-axis at 120 Ma and corresponds to a rifting period from 130-120 Ma. The first blue dot corresponds to a rifting period from 200-120 Ma. The dashed blue line shows $z_{LAB,init}$ based on isostatic balance of Figure 1.

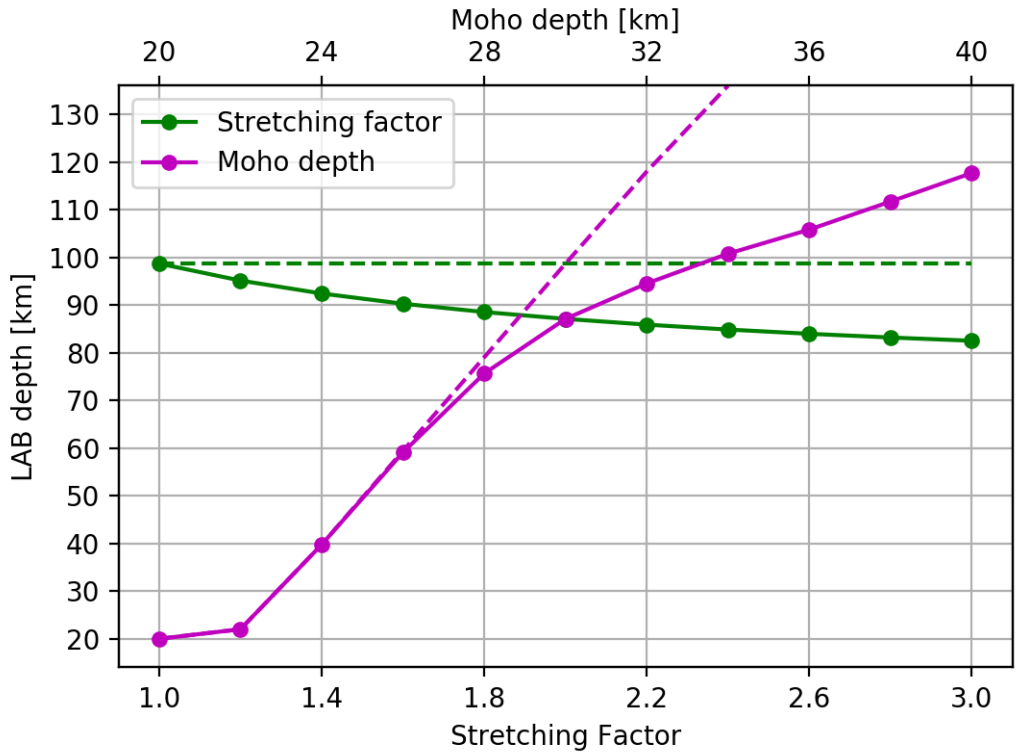

Figure 5. Stretching factor and Moho depth vs. LAB depth. The solid green line indicates $z_{LAB,rifted}$ for varying stretching factors *ß* between 1-3, while the solid magenta line shows $z_{LAB,rifted}$ for variable initial crustal thickness between 20-40 km. The dashed lines represent LAB depths of the initial isostatic balance.

4 Results

4.1 LAB for the South American passive margin

Figure 6 shows $z_{LAB,rifted}$ for the South American passive margin. The South American passive margin can be split into an equatorial and a southern part, separated by the Chain Fracture Zone. $z_{LAB,rifted}$ varies from values locally lower than 50 km to deeper than 200 km. Remarkably, there are also large gradients of $z_{LAB,rifted}$ between the inner and outer COB. The magnitude depends on the distance between inner and outer COB. For example, in the Pernambuco-Parnaiba Basin $z_{LAB,rifted}$ varies ~100 km between inner and outer COB as the inner COB extends deeply into the Borborema Province.

The sedimentary basins south of the Chain Fracture Zone have been formed during early opening of the South Atlantic. In this area, $z_{LAB,rifted}$ is characterized by a rather heterogeneous structure with values mostly lower than 100 km. Locally, there are large horizontal gradients, causing strong deviations of the lithospheric thickness even inside a single sedimentary basin. Very shallow lithosphere can be observed in the Campos, Santos, Punta del Este, and Colorado Basins with values lower than 50 km, indicating strong deformation due to high stretching factors. The shallow lithosphere of the Campos and Santos Basins is intersected by a thick lithospheric piece in the southern Santos and northern Pelotas Basin. Here, $z_{LAB,rifted}$ reaches values up to 160 km even towards the outer COB.

In contradiction to the southern part, $z_{LAB,rifted}$ reveals a rather smooth structure between 100-150 km in the equatorial part of the South American passive margin. Even though the deforming region of the equatorial segment is narrower than for the southern segment, for most basins a high gradient of lithospheric thickness between inner and outer COB is present with thinning towards the outer COB.

Most features of $z_{LAB,rifted}$ are already present in the isostatically derived $z_{LAB,init}$ (Figure 7a). However, in the equatorial part, the gradient of lithospheric thickness between the inner and outer COB is higher than for $z_{LAB,rifted}$. The difference between $z_{LAB,init}$ and $z_{LAB,rifted,}$ $\Delta z_{LAB,}$ shows that in this area rifting causes more variety than for other parts of the margin (Figure 7b). Δz_{LAB} has a maximum of 12 km, with the highest values in the Borborema Province, which is the onshore continuation of the Pernambuco-Parnaiba and Sergipe-Alagoas Basins, and in the Pelotas and Santos Basins offshore of Brazil. For other regions Δz_{LAB} is mostly lower than 7 km.

A cumulative plot of $z_{LAB,init}$ versus Δz_{LAB} follows a Gaussian distribution with a standard deviation of 22.5 km (Figure 8). Δz_{LAB} reflects the behavior of the geotherms as shown in Figure 2. The isostatic equation (Eq. 1) shows that thin lithosphere correlates with thin crust. If both layers are thin, Δz_{LAB} has no time to propagate and is negligible for lower values of $z_{LAB,init}$. Thick crust correlates with thick lithosphere. In this case, the geotherms deviate from each other in deeper levels which cannot be compensated by the mantle lithosphere. Consequently, Δz_{LAB} gets small for higher values of $z_{LAB,init}$ (Figure 8). Selecting Δz_{LAB}= 5 km as a benchmark shows that only a range of 110-170 km for $z_{LAB,init}$ cause deviations of $z_{LAB,rifted}$ during the rifting process. The maximum of the curve corresponds to $z_{LAB,init}$=135 km and Δz_{LAB}=10 km.

Figure 9a displays the mantle density of the isostatic column prior to rifting. Notably, ρ_m is 3.35 g/cm³ for most areas. The difference to ρ_a (3.3 g/cm³) is 0.05 g/cm³ and reflects the temperature-dependent decrease of density with depth from lithosphere to asthenosphere. The outermost Campos and Santos Basins show anomalous minima of ρ_m around 3.31-3.32 g/cm³. These structures partly require a higher number of iterations that are needed to satisfy the density threshold criterium (Figure 9b).

Most of the points in Figure 9b reach the density threshold after i <=4 iterations. Only where lithospheric thickness is very shallow, the algorithm needs more time to converge. This shows an inherent stability between mantle density and thickness of the mantle lithosphere, which are the variable parameters of our inverse approach.

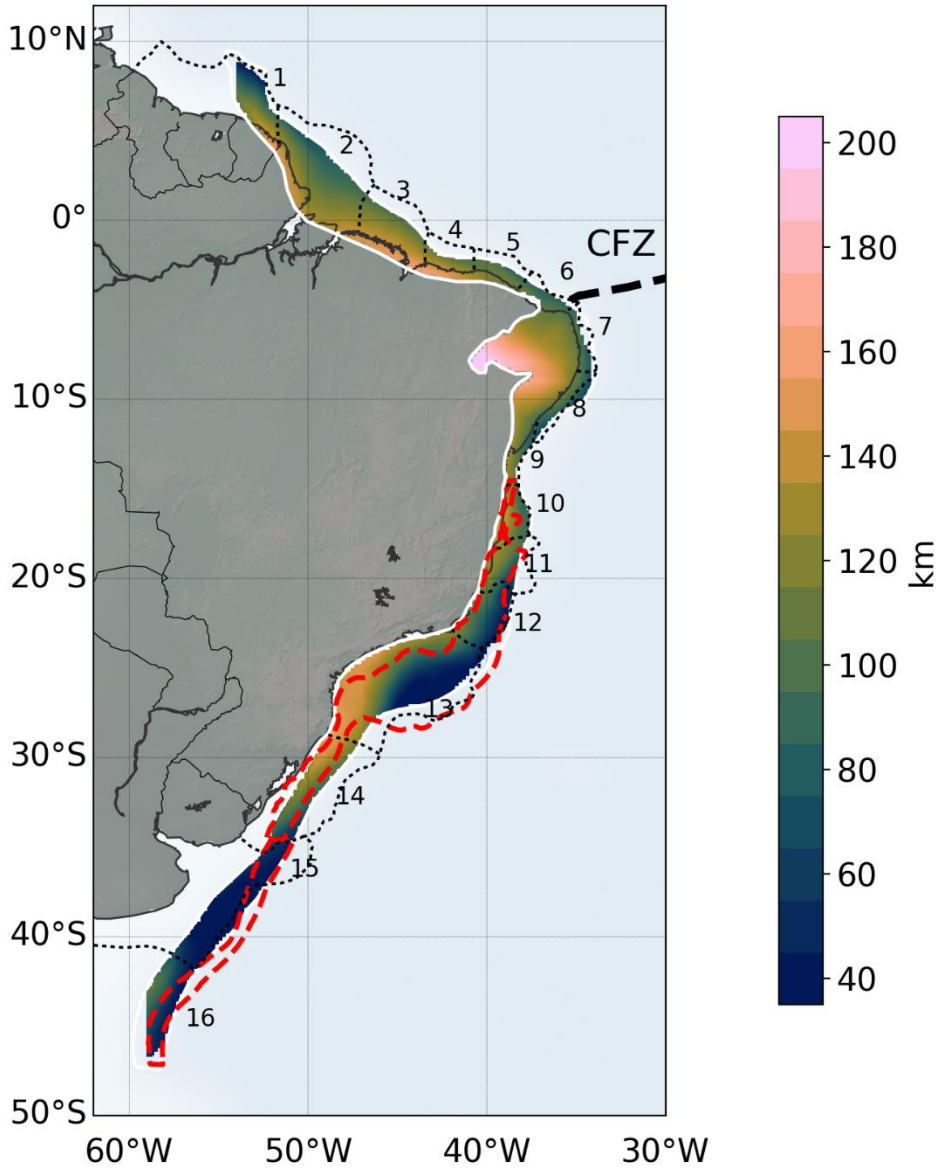

Figure 6. LAB after rifting at the passive margin of South America. Thick dashed black line indicates Chain Fracture Zone (CFZ). Thick dashed red polygon marks the extension of Large Igneous Provinces (LIPs) offshore South America, taken from the Johansson et al. (2018) data base. Dashed contours and numbers indicate offshore sedimentary basin locations, taken from Wen et al. (2019). 1: Guyana, 2: Foz do Amazonas-Marajo, 3: Para-Maranhao, 4: Barreirinhas, 5: Ceara, 6: Potiguar, 7: Pernambuco-Parnaiba, 8: Sergipe-Alagoas, 9: Bahia Norte, 10: Bahia Sul, 11: Espirito Santo, 12: Campos, 13: Santos, 14: Pelotas, 15: Punta del Este, 16: Colorado.

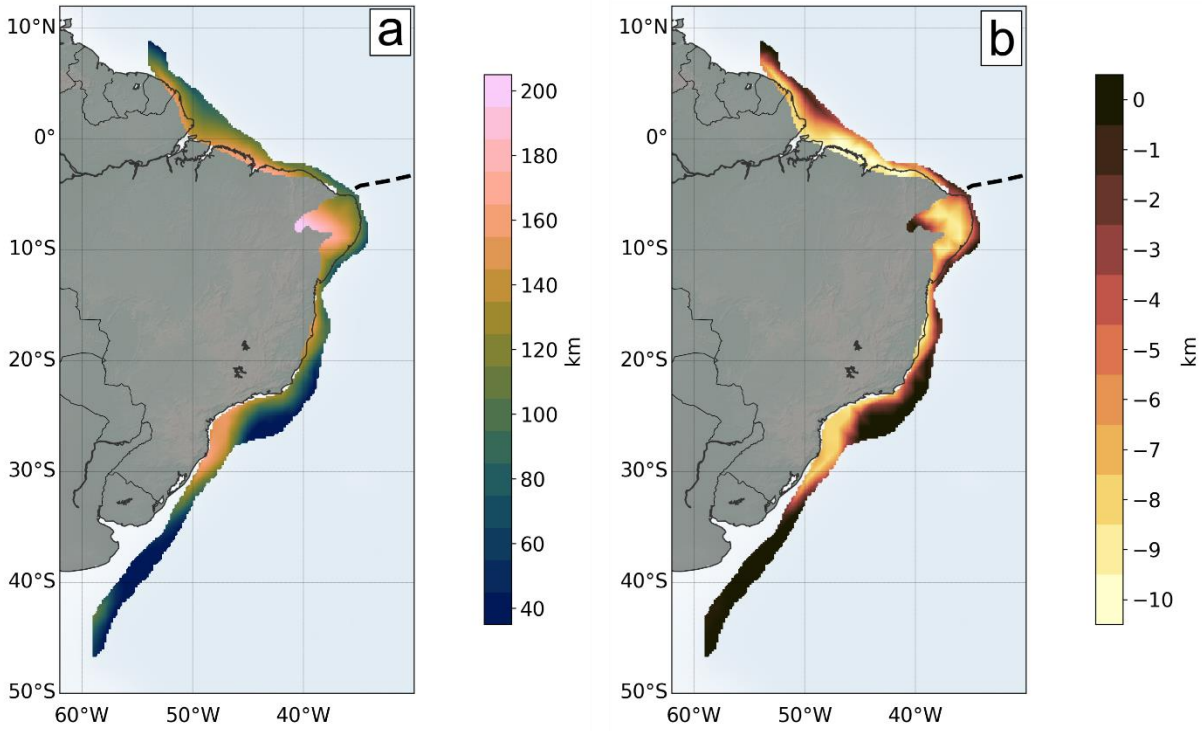

Figure 7. a: Initial isostatic LAB before rifting, **b**: Difference of LAB before and after rifting. Dashed line indicated Chain Fracture Zone.

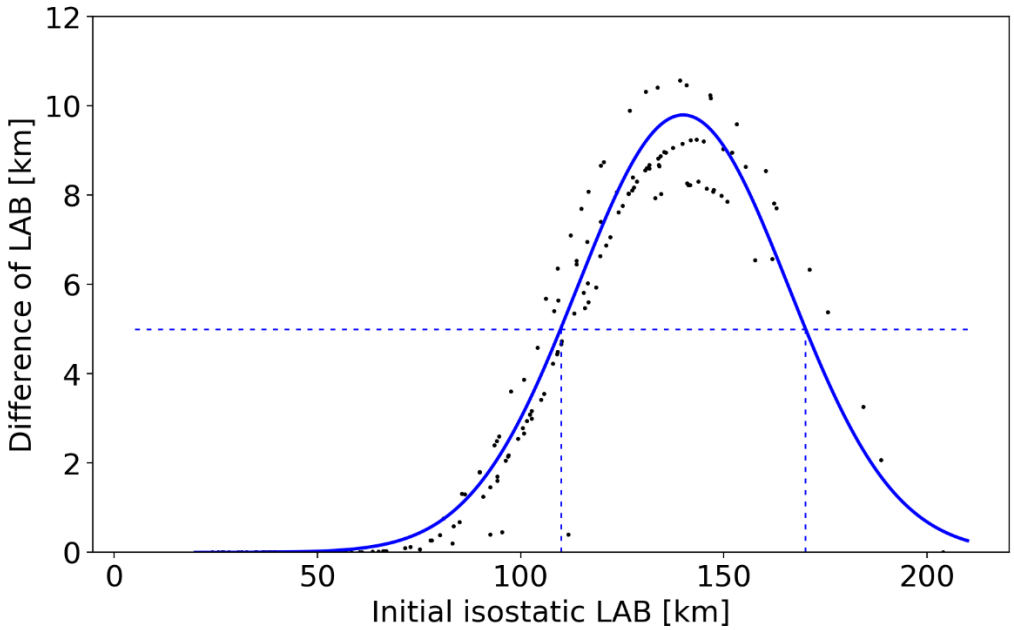

Figure 8. Distribution of Initial Isostatic LAB vs. Difference of LAB before and after rifting. The horizontal dashed line indicates the difference benchmark of Δz_{LAB}= 5 km.

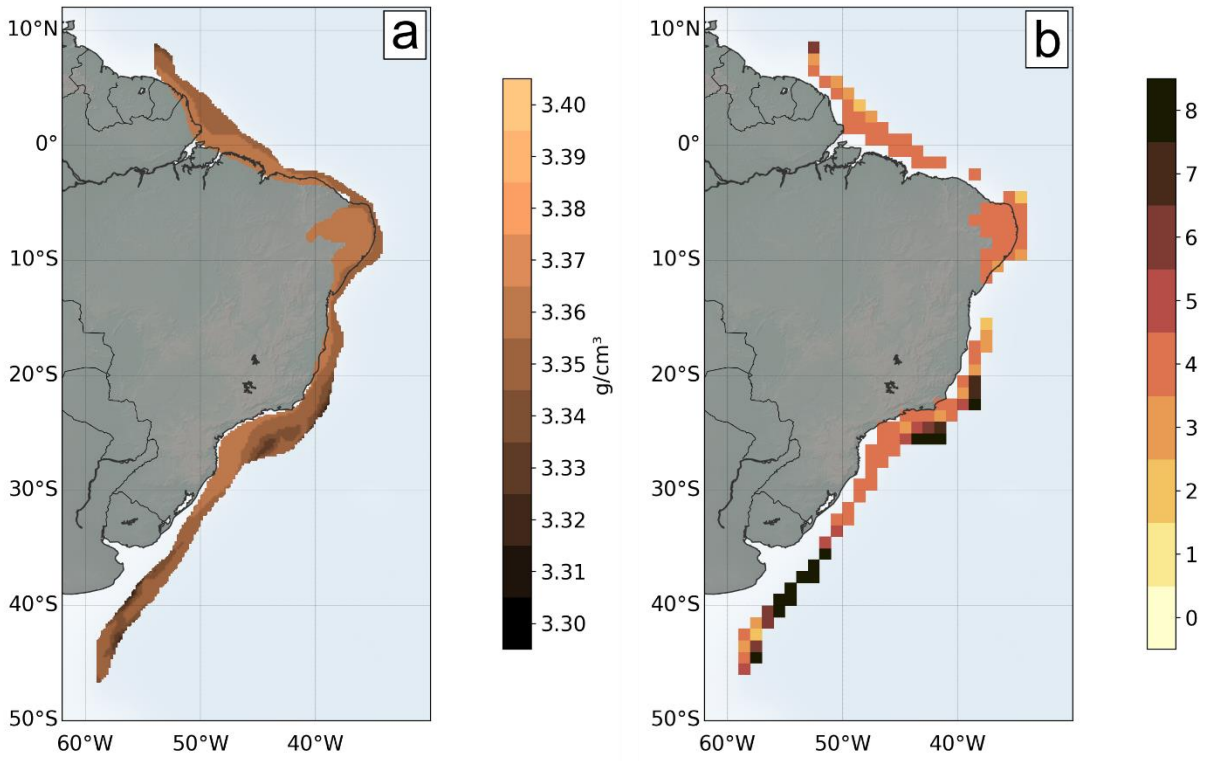

Figure 9. a: Mantle density before rifting, **b**: Number of iterations needed to satisfy density fit. Note that the resolution is kept to 1 degree to show the convergence at each point of the grid.

4.2 LAB of the conjugate South Atlantic passive margins in a Western Gondwana framework

We used the same approach to calculate $z_{LAB,rifted}$ for the African passive margin (see supporting information S2 for the crustal model, segments of crustal thickness, and stretching factors). Figure 10 shows $z_{LAB,rifted}$ in a Gondwana framework, rotated to 83 Ma while the entire South Atlantic had been opened. The conjugate margins between Ascension and Rio de Janeiro Fracture Zone are connected by flowlines, which have been calculated by a set of seed points located on the Mid Atlantic Ridge. The flowlines are used to calculate the width of the passive margins.

In many parts of the African passive margin, the width is less than on the conjugate South American side, especially in the African equatorial segment. However, the general trend of deeper lithosphere in the equatorial segment and shallower lithosphere in the southern segment is also observed at the African passive margin. A notable difference appears at the northernmost tip of the African deforming region, where the lithospheric thickness is shallower than 50 km.

For the central part of the African passive margin, the lithospheric thickness is less variable than for South America. The thickness is mostly lower than 100 km with lowest values offshore Congo and Kwanza Basin. In this area, the passive margin appears to be wider than for the South American counterpart, suggesting more constant lithospheric thinning. The across-margin gradients are not as pronounced as for the South American passive margin since $z_{LAB,rifted}$ is already quite shallow towards the inner COB.

In the southern part, where the African passive margin is rich in volcanic material, the lithospheric thickness shows intermediate values ~100 km towards the inner COB. The across-

margin gradient is relatively high with values lower than 50 km towards the outer COB. Compared to the South American counterpart, the African side shows less along-margin heterogeneity.

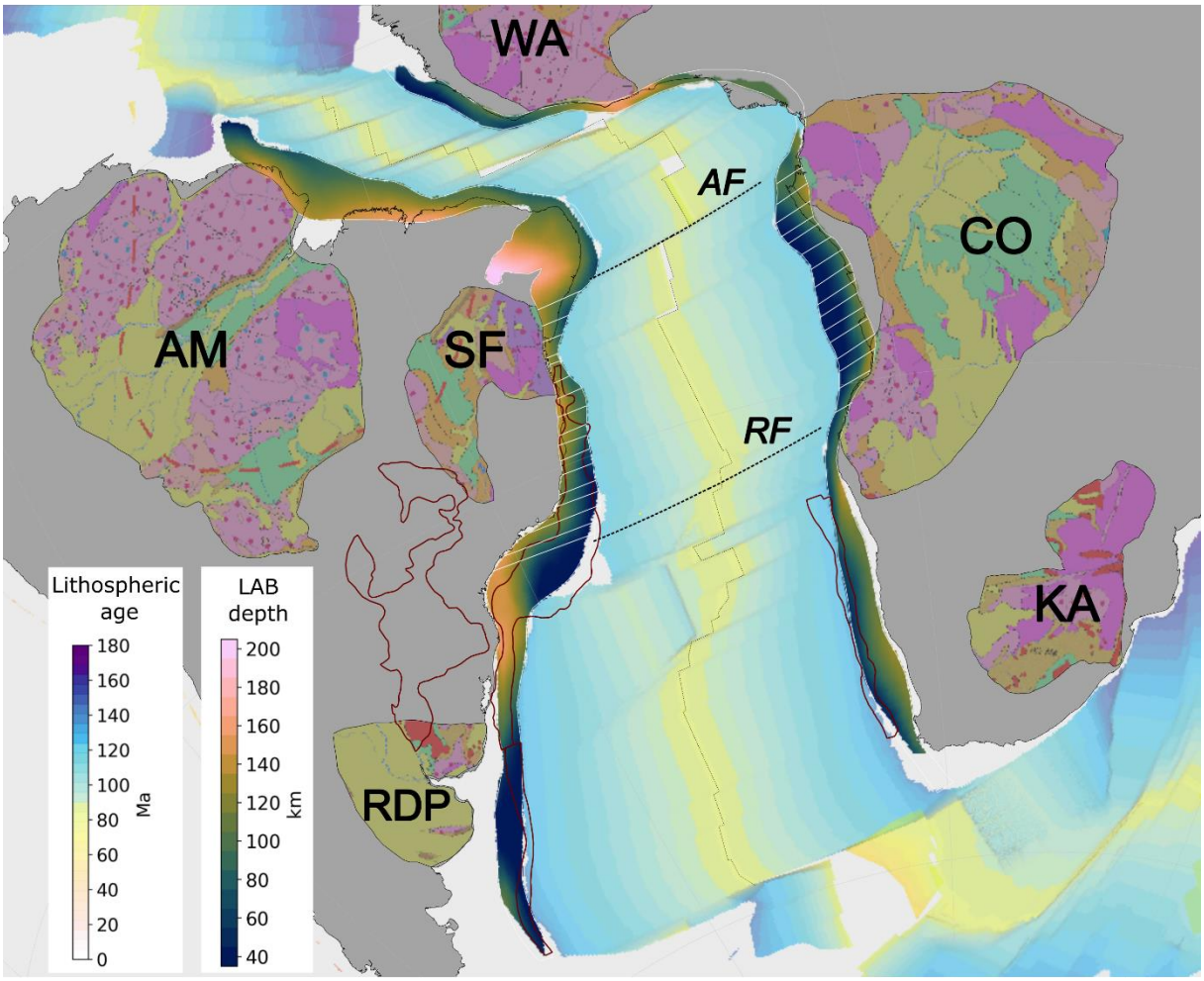

Figure 10. Lithospheric thickness for the deforming region of the South American and African passive margins in Gondwana framework, rotated back to 83 Ma using GPlates software (Müller et al., 2018). In between, the age of the oceanic lithosphere is visualized (Seton et al., 2020). Thin dashed line represents the location of the Mid Atlantic Ridge at 83 Ma. AF=Ascension Fracture Zone, RF=Rio de Janeiro Fracture Zone. Grey lines represent flowlines intersecting the passive margins and are used to calculate margin width (see Fig. 12-14). Cratons on the continent are draped with geology. Craton boundaries are taken from Celli et al. (2020). Cratonic units are abbreviated: AM=Amazonia, SF=Sao Francisco, RDP=Rio de la Plata, WA=West Africa, CO=Congo, KA=Kalahari. Dark red polygons show location of LIPs, taken from the Johansson et al. (2018) data base.

5 Discussion

5.1 The role of magmatic underplating for the LAB structure along the South Atlantic passive margins

The two-part lithospheric structure with deeper lithosphere in the equatorial part and shallower, more heterogeneous lithosphere in the southern part along the South American passive margin offers insights in the rifting mechanism that controlled the break-up of Pangea. The smooth lithosphere at the equatorial margins, especially on the South American side, implies that far-field edge forces are the dominant mechanism, causing only minor thinning of the pre-break-up continental lithosphere. The lithospheric thickness is in a range that can be expected for stable continental platforms (e.g., Artemieva, 2012). A lower amount of lithospheric thinning indicates that less magmatic material has been involved in the rifting process. This is the case for the equatorial passive margin of South America, where LIPs are absent.

At the southern part of the passive margins the initial lithosphere has been thinned more extensively. This suggests a longer initial slow pre-rift phase with sufficient time to destruct the initial continental lithosphere. In some areas, like the Colorado Basin on the South American side, the LAB is even shallower than 50 km. Such a shallow LAB is rather unlikely and is a result of the assumed simplifications governing the initial isostatic equation.

The heterogeneous lithospheric structure of the southern South American margin points to a more variable rifting process, which is strongly connected to underplating of magmatic material. On the one hand, magmatic underplating thickens the crust by adding partial melts from a stable magma chamber to the base of the crust and cooling over a longer time period (e.g., Cox, 1993; Thybo and Artemieva, 2013). On the other hand, crustal thickening due to magmatic underplating might not necessarily be an indicator for lithospheric thickening or thinning.

The occurrence of LIPs (see polygons in Figures 6 and 10) shows that the bulk of the southern margin has been affected by volcanic underplating. In the Colorado Basin, volcanic underplating is associated with SDRs. McDermott et al. (2018) distinguish the SDRs in this area in two different types, representing the continuum from continental rifting to full plate separation with formation of new magmatic crust. While the first type was formed during stretching of the crust, the second type was formed as narrow lava flows due to the Tristan plume activity (McDermott et al., 2018). Even though the passive margin does not capture the entire sequence of SDRs, the modeled lithospheric thickness is characterized by very low values in this area. A transition of two different SDR types cannot be observed in terms of lithospheric thickness.

According to McDermott et al. (2018) SDRs smoothly transition from combined passive continental rifting/plume activity to wider lavas, representing magmatic activity only. This transition zone is located offshore Uruguay/Brazil in the Pelotas Basin and correlates with a distinct transition of lithospheric thickness over a relatively short distance. While increased plume activity induces reinforced lithospheric thinning, our model shows the opposite behavior as the LAB increases from ~40 km to ~100 km under the Pelotas Basin (Figure 6).

Morgan et al. (2020) showed that the formation of the volcanic rifted margins in the South Atlantic is a result of an asymmetric lateral drainage of the Tristan Plume. This asymmetric flow is triggered by along-strike variations in the geometry and opening of the rift, as well as lateral variations in the initial continental lithosphere. In the initial model setup, cratons are assumed to have thicker lithosphere than the surrounding regions. Using 3D numerical modeling, this structure is roughly preserved throughout the first 28 Ma of rifting (see Figure 3 and S4 in Morgan et al., 2020). The shallower lithosphere in the Morgan et al. (2020) model pulls the plume material southwards and coincides with the deeper lithosphere in the Santos and Pelotas Basins, as featured in our model.

Both the SDR distribution as observed by McDermott et al. (2018) and the model of lateral plume drainage of Morgan et al. (2020) do not match our observation of deep lithosphere in the

Santos and Pelotas Basins. This raises two general questions regarding our modeled LAB: 1. Can small-scale patterns like different types of SDR be identified and distinguished? 2. Can larger-scale patterns that arise from plume-rift interaction be identified and distinguished?

SDRs are an indicator of increased magmatic activity. They are emplaced at a narrow time window in the synrift phase, whereas the underlying lithosphere can be modified over a much longer time frame afterwards. The distribution of SDRs points to different melting mechanisms in the lithosphere. Even though SDRs represent different episodes of lithospheric thinning, their size is too small to be recovered by our lithospheric model.

The lithospheric structure of the Morgan et al. (2020) model at the Santos and Pelotas Basins is controlled by two parameters: location of the starting plume head and definition of the initial lithospheric thickness. Morgan et al. (2020) showed that different plume locations and plume fluxes do not impede southward migration of plume material (see their supplementary material). The shallow lithosphere in their model, located in the Santos and Pelotas Basin, is a combination of both parameters, but always based on a certain assumed geometry. Varying the initial geometry would cause a different pattern of the initial lithosphere.

Qualitatively, our LAB model distinguishes patterns of both SDRs and location of volcanic material during rifting. Quantitatively, we cannot correlate our LAB model with different SDR types and the asymmetric plume flow, as observed by Morgan et al. (2020). Thus, the amount of volcanic material emplaced during rifting and plume activity remains enigmatic.

5.2 Comparison of stretching factors

The stretching factors of Müller et al. (2019) serve as a basis to define a global deforming plate motion model. The total stretching factor is defined by stacking all stretching factors over time for a certain point or area. This is beneficial when multiple rifting or collisional events occurred. As the stretching factors of Müller et al. (2019) are valid for plate motions since the Triassic, the opening of the South Atlantic is the only event contributing to the stretching factors. Müller et al. (2019) showed that globally most extensions range in stretching factors $\beta=1\text{-}2$. Stretching factors larger than 2 reflect highly extended areas.

In Figure 11a the total stretching factors β for the South American passive margin are plotted. The stretching factor β varies between 1-3, indicating extensional tectonics only. Both the equatorial and southern passive margins comprise a heterogeneous distribution. The Amazonas-Marajo Basin in the north and Bahia Basin, Espirito Santo Basin and Campos Basin in the south show highest values of stretching larger than 3.

Rescaling the stretching factors of our approach (Figure 3c) to the same amplitude as in Figure 11a reveals a considerably lower amount of stretching (Figure 11b). The pattern of stretching with the two-part structure of lower stretching in the equatorial segment and higher stretching in the southern segment is less pronounced. However, the highest stretching factors in the Campos and Santos Basins ($ß=2$) correlate with the distinct area of high stretching in Figure 11a ($ß>=3$). Other similarities are the lower stretching factors in the Pernambuco-Parnaiba Basin and adjacent Borborema Province, as well as the varying pattern in the Punta del Este and Colorado Basin further south.

The high stretching factors of the Müller et al. (2019) model imply that crustal thickness of unthinned crust is more than three times larger than thinned crust. Our model does not reflect such high values due to averaging of the continental crust into certain segments (Figure 3a and 3b). In Müller et al. (2019), crustal thickness prior to extension is defined by seismological

measurements along a given zone of extension, causing higher variability of the initial crustal thickness and consequently locally higher stretching factors.

The underlying plate deformation in the Müller et al. (2019) plate motion model is approximated by a pure-shear, uniform extension model. As this is the only way to define a kinematic plate model without capturing ductile flow, rift-internal variations of stretching, representing strain localization or depth-dependent stretching, are not included. As a consequence, the stretching factors represent "wide rifts that lack margin-orthogonal strain rate and crustal thickness gradients" (Müller et al., 2019). In Figure 11a this becomes obvious as the pattern of stretching varies only along strike. The stretching factors of our approach are derived independent of a plate motion model by the crustal thickness model only. They comprise heterogeneities of the crustal model as margin-perpendicular and margin-alongside gradients.

In Müller et al. (2019), the thinned crust is defined by integrating a surface dilatation rate over time. This may be a source of error because the dilatation rate is not exactly known at each time step. We approximate the recent crustal thickness in the deformable region as thinned crust. This method might be another source of error because not each crustal unit of the deformable region represents thinned crust due to rifting only but might be thickened by magmatic underplating as well. Less underplating would cause lower crustal thickness in the passive margin and higher stretching factors.

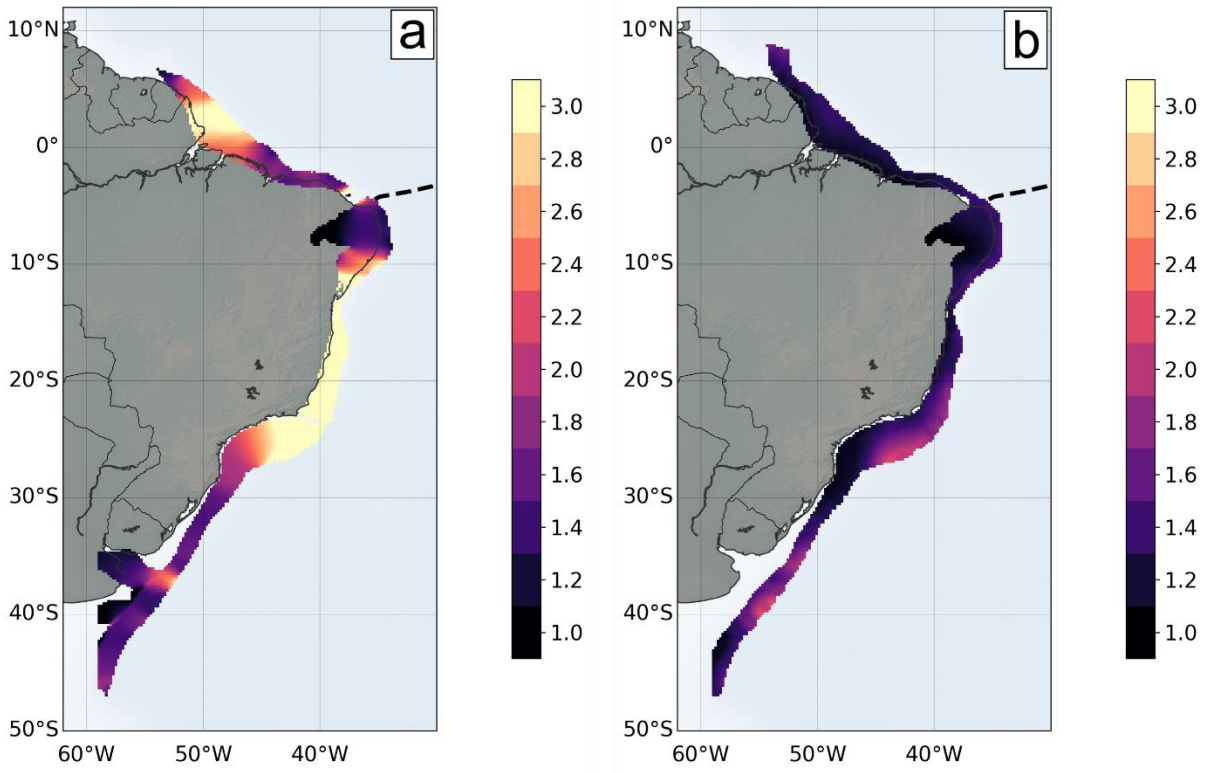

Figure 11. Stretching facors along the South American passive margin. **a**: Stretching factors of Müller et al. 2019, **b**: Stretching factors of this study

5.3 Relation of lithospheric thickness and passive margin width

The South Atlantic passive margins are strongly related in age. While classical 2D-rifting models like McKenzie (1978) suggest uniform extension of both margin sides, recent studies showed that initial rift asymmetry leads to different widths of conjugate margins (Brune et al., 2014). This is also reflected in the deforming regions of the Müller et al. (2019) plate motion model. Comparing the lithospheric thickness of both margin sides can be an indicator of how much lithospheric thinning has contributed to rift asymmetry.

We used the conjugate Bahia/Espirito Santo/Campos Basins on the South American side and the (offshore) Congo/Kwanza Basins on the African side to study the lithospheric thickness of both margins jointly because the asymmetry of conjugate margin width is particularly pronounced in this area. Using flowlines, the difference is determined by subtracting the lithospheric thicknesses at the outer COB of conjugate margin pairs. The width of a passive margin is calculated by shifting flowlines, propagating from the Mid Atlantic Ridge, towards the inner COB of the respective passive margin (see Figure 10).

The conjugate margins are characterized by large differences in the lithospheric thickness (Figure 12). In the northern Bahia and Congo Basins the difference is moderate with 20 km deeper lithosphere in the Congo Basin. For the southern Bahia/Congo Basins this changes abruptly. Here, the LAB is 80 km deeper in the South American Bahia Basin, coincident with distinct narrowing of the margin. This pattern proceeds throughout the Espirito Santo/Lower Congo Basins with 50-60 km thicker lithosphere at the South American margin. For these particular conjugate basins, a considerable amount of magmatic underplating has been mapped on the South American side (Johansson et al., 2018), whereas these structures are absent on the African side. Towards the Campos/Kwanza Basins the lithospheric thickness pattern gradually changes to 30 km thinner lithosphere at the South American margin. This part of the Campos Basin is characterized by a very wide margin, while the Kwanza Basin narrows towards the Rio de Janeiro Fracture Zone.

Plotting the differences of LAB depth and margin width against each other shows a linear correlation of both parameters (Figure 13). Locally, the South American margin is up to 600 km wider than the African conjugate. That is because the wide extension of the Campos Basin is amplified by an oblique distribution of the flowlines. In this area, the South American lithosphere is up to 40 km thinner than the African lithosphere. Following the linear trend shows that up to 20 km shallower South American LAB occurs for margin width differences between ±100 km, independent of the margin side. For the narrower South American margin, the linear trend of increasing lithospheric thickness difference is more distinctive than for the wider margin. A maximum difference of -200 km in margin width correlates with 80 km deeper LAB for the South American margin.

The highest LAB differences are found in the Bahia Basin, where the passive margin is locally narrower than 100 km. In this area, the across-margin gradients of lithospheric thickness are less pronounced, causing a relatively deep LAB at the outer COB (Figure 6 and Figure 10). Possible magmatic underplating could have strengthened this effect. The African conjugate shows a very shallow LAB, mainly caused by shallow crust and high stretching factors in the deforming region. Besides that, no magmatic underplating has been mapped. Even for the narrow margin in the southern Kwanza Basin the LAB is rather shallow, causing only moderate differences in lithospheric thickness for the conjugate margin pairs.

A contribution of magmatic underplating to lithospheric thinning cannot be defined by our models. But they show that magmatic underplating might not necessarily be accompanied by extensive melting at the lithospheric base. Our results suggest that the asymmetry of the rifts

rather causes differences in lithospheric thickness of both margins. However, this is only valid for a scenario where lithospheric thickness is initially constant for both margin sides. Our initial isostatic LAB could be regarded as pre-Gondwana-breakup, but its amplitude is too close to our final model. However, establishing a LAB model in a Gondwana framework is beyond the scope of this paper.

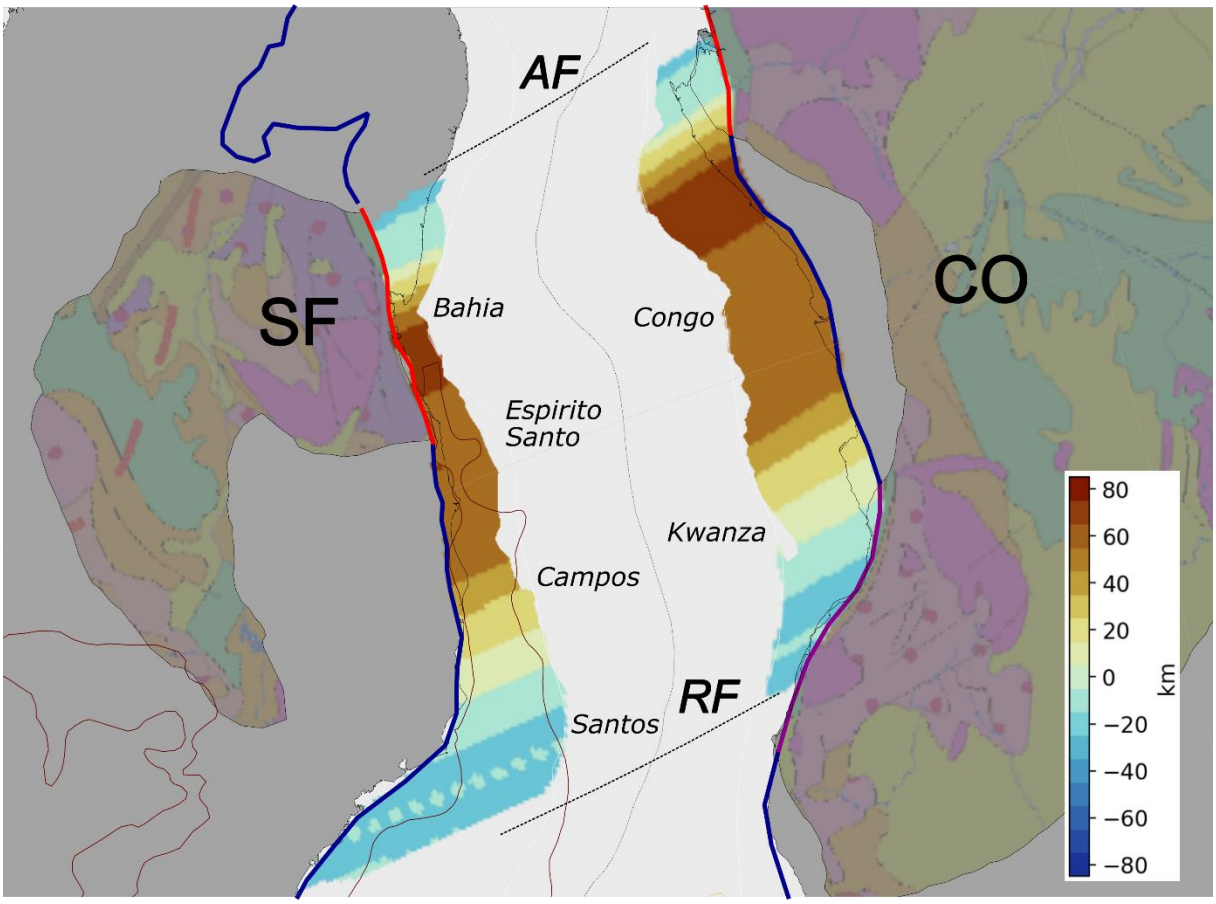

Figure 12. Difference of lithospheric thickness for selected conjugate South American and African basins, rotated back to 105 Ma. Red colours indicate deeper LAB in South America, blue colours deeper LAB in Africa. Thick lines at the inner COBs indicate directly adjacent cratons (Red: Sao Francisco and northern Congo Craton, purple: Southern Congo Craton, Blue: No craton adjacent). Red polygons indicate LIPs, for abbreviations see Figure 10.

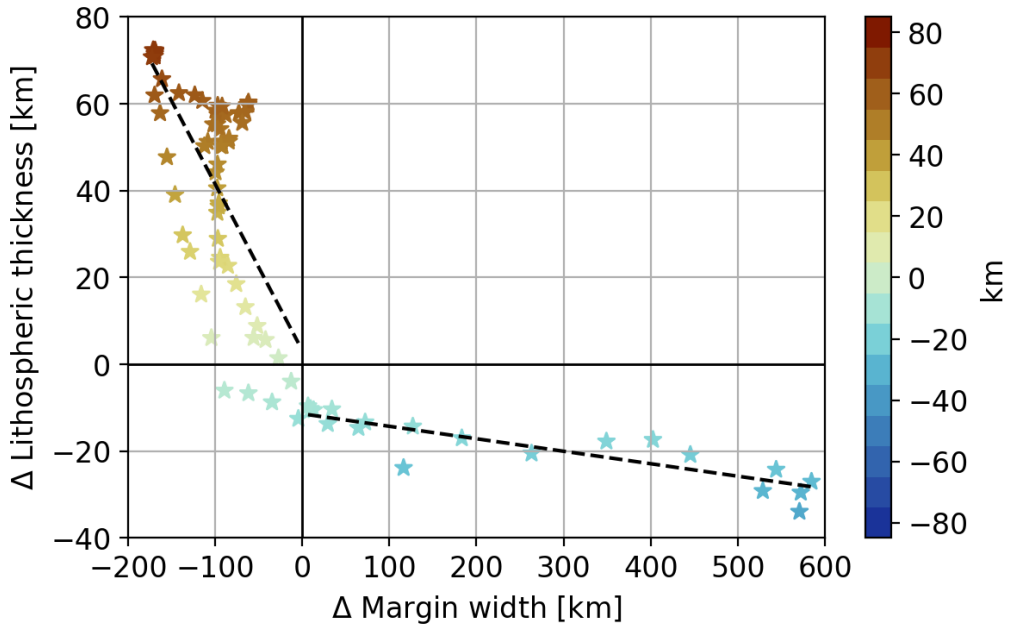

Figure 13. Difference of margin width of conjugate margin pairs versus difference of lithospheric thickness at the respective points at the outer COB. Red colours indicate deeper LAB in South America, blue colours deeper LAB in Africa. Dashed lines show the linear fit for the pairs with wider African margin (negative Δ Margin width) and for the pairs with wider South American margin (positive Δ Margin width). Colour map is same like in Figure 12.

5.4 The role of cratons and Parana Flood Basalts for lithospheric thickness in deforming regions

Distinguishing the individual lithospheric thickness and margin width for the margin segments per continent shows a linear trend that is surrounded by several outliers (Figure 14). To investigate how much the cratons contribute to these deviations, we marked each point by colors. For the South American margin, thicker lithosphere occurs in the vicinity of the Sao Francisco Craton, which is also characterized by narrow margin widths (Figure 14a).

For the African side, we distinguish between the southern and northern Congo Craton. Together with the area where the southern Congo Craton reaches the coastline the points outside the craton boundary form a linear trend. Stronger deviations belong to those points, where the northern Congo Craton intersects the deforming region. Overlapping geometries of the craton and deforming region can introduce errors in the modeled lithospheric thickness. In this case, unthinned crust contains some portions of cratonic lithosphere. Consequently, stretching is underestimated, which causes subsequent overestimation of the lithospheric thickness. This trend can clearly be reproduced in the distribution of the outliers (Figure 14b).

The profiles of margin width versus lithospheric thickness for both continents evince that the location of the cratons controls the LAB depth. Deeper values of LAB are preferably observed in areas, where the inner COB reaches the craton. In the south, the Parana Flood Basalts are located between the Sao Francisco and Rio de la Plata Cratons. In this area, the deep LAB in the adjacent Santos and Pelotas Basins reflects high stretching factors and a strong contrast between unthinned and thinned crust (Figure 6). Our interpretation is that the relatively short, but intense magmatic activity, forming the Parana Flood Basalts (Thiede and Vasconcelos, 2010), caused a

crustal thickening in the area of the Parana Basin. This can also be seen in Figure 3b, where the average crustal thickness of the Parana Basin is similar to the cratons. However, in the deforming region, the volcanic activity occurred in a later stage and lead to rifting with crustal and lithospheric thinning.

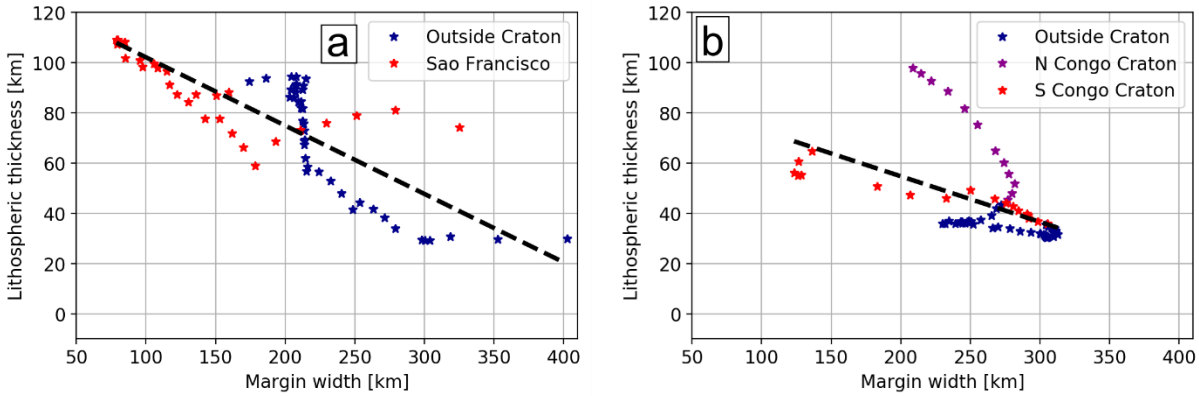

Figure 14. Margin width of conjugate margin pairs versus lithospheric thickness for the individual passive margins. Linear trend is visualized as black dashed line. **a:** South America, **b:** Africa

6 Conclusions

We have derived a new thermal lithospheric thickness model for the South Atlantic passive margins. Our model is calculated as a function of rifting time, crustal thickness, and stretching factor. The stretching factors are obtained by the amount of unthinned crust divided by thinned crust, using state-of-the-art crustal models for the South American and African continent. The new stretching factors account for across rift crustal gradients at the passive margin and are a refinement compared to the Müller et al. (2019) model.

From our model, the lithospheric structure of the conjugate passive margins can be distinguished in two parts: the equatorial part with deep lithosphere along the relatively narrow margins and the southern part with rather thin lithosphere. For the South American passive margin, the lithospheric thickness reveals a very heterogeneous structure, which can be related to different rifting mechanisms that lead to the opening of the South Atlantic. Magmatic underplating and SDRs indicate more complex tectonics with a large amount of volcanic material, which is reflected in the heterogeneous LAB depth. The subsequent equatorial opening of the South Atlantic, driven by far-field forces, is evident in a minor destruction of the initial continental lithosphere. For Africa, the lithospheric thickness is rather shallow along the entire margin.

Analyzing the lithospheric thickness in a Western Gondwana framework evinces its large variability in conjugate basins of the South American and African passive margins. The differences in lithospheric thickness are up to 80 km. We propose that these differences reflect highly asymmetric melting and lithospheric thinning prior to rifting. This is also in accordance with the margin widths. Wider margins have higher across gradients and a shallower LAB at the outer COB compared to conjugate basins of the other margin. This asymmetry is manifested in the different distribution of margin width and lithospheric thickness for each continental margin.

Our modeling approach does not capture the amount of melting and volcanic underplating. This is reflected in very shallow LAB regions in the southern passive margins. The mechanism of underplating control on lithospheric thickness cannot be resolved by our model. Furthermore, the

lithospheric thickness strongly depends on the initial crustal model and the governing isostatic equation. Despite these simplifications, our LAB model represents the thermal state of the rifted margins at present day, which generally agrees with other studies.
Future efforts should focus on including melting and magmatic underplating, once a comprehensive data set outlining underplated crustal thickness on both conjugate margins is available. This could be easily included in the governing isostatic equation. The modeling of the thermal structure can be extended to 2D rifting scenarios instead of the 1D approach that we are using. Given the potential of improvements, we are confident that our approach opens a new pathway for more extensive analysis of the lithospheric structure of passive margins. Our procedure can be easily extended to other passive margins on the globe. Ultimately, this would fill the gaps of reconstructed lithospheric models for the Gondwana Supercontinent.

Acknowledgments

This work has been funded by the Deutsche Forschungsgemeinschaft (DFG) within the project 'Linking the deep structures of the cratons of Africa and South America by integrated geophysical modelling' (project number 336717379).
We thank Nicky White from University of Cambridge for sharing his FORTRAN code, which has been converted to Python by Michael Chin from University of Sydney. Gregory Houseman from Leeds University is thanked for his contributions to the code and for general discussions about thermal modeling. Furthermore, we thank Paul Bellingham from ION Geophysical for fruitful discussions on modeling lithospheric extension along passive margins.
Most of the plots have been created using Matplotlib with color-blind friendly color maps provided (Crameri, 2018; Hunter, 2007).
We are thankful for the valuable comments of the reviewers.

Data

Models of crustal thickness and density for South America are published via the GFZ Data Services: https://doi.org/10.5880/GFZ.1.3.2020.006 (Finger et al., 2021). For Africa, the data is in preparation. The rifting times of the South Atlantic opening are part of the deforming plate model of Müller et al. 2019, which is available at:
https://www.earthbyte.org/webdav/ftp/Data_Collections/Muller_etal_2019_Tectonics/
A version of the code RiftSubsidence.py that generates the presented results will be made available for the public. This code will be distributed, probably with GitHub, within the final submission of the manuscript.

References

Afonso, J. C., Salajegheh, F., Szwillus, W., Ebbing, J. & Gaina, C. (2019): A global reference model of the lithosphere and upper mantle from joint inversion and analysis of multiple data sets. In: *Geophysical Journal International* 217 (3), S. 1602–1628. DOI: 10.1093/gji/ggz094.
Artemieva, I. M. (2012): A lithospheric perspective on structure and evolution of Precambrian cratons. In: Phanerozoic Regional Geology of the World: Elsevier, S. 94–111.
Blaich, O. A., Faleide, J. I. & Tsikalas, F. (2011): Crustal breakup and continent-ocean transition at South Atlantic conjugate margins. In: *J. Geophys. Res.* 116 (B1), S. 9. DOI: 10.1029/2010JB007686.

Bown, J. W. & White, R. S. (1995): Effect of finite extension rate on melt generation at rifted continental margins. In: *J. Geophys. Res.* 100 (B9), S. 18011–18029. DOI: 10.1029/94JB01478.
Brune, S., Heine, C., Pérez-Gussinyé, M. & Sobolev, S. V. (2014): Rift migration explains continental margin asymmetry and crustal hyper-extension. In: *Nature communications* 5, S. 4014. DOI: 10.1038/ncomms5014.
Brune, S., Williams, S. E. & Müller, R. D. (2017): Potential links between continental rifting, CO2 degassing and climate change through time. In: *Nature Geosci* 10 (12), S. 941–946. DOI: 10.1038/s41561-017-0003-6.
Brune, S., Williams, S. E. & Müller, R. D. (2018): Oblique rifting. The rule, not the exception. In: *Solid Earth* 9 (5), S. 1187–1206. DOI: 10.5194/se-9-1187-2018.
Buiter, S. J.H. & Torsvik, T. H. (2014): A review of Wilson Cycle plate margins. A role for mantle plumes in continental break-up along sutures? In: *Gondwana Research* 26 (2), S. 627–653. DOI: 10.1016/j.gr.2014.02.007.
Celli, N. L., Lebedev, S., Schaeffer, A. J. & Gaina, C. (2020): African cratonic lithosphere carved by mantle plumes. In: *Nature communications* 11 (1), S. 92. DOI: 10.1038/s41467-019-13871-2.
Cox, K. G. (1993): Continental magmatic underplating. In: *Phil. Trans. R. Soc. Lond. A* 342 (1663), S. 155–166. DOI: 10.1098/rsta.1993.0011.
Crameri, F. (2018): Geodynamic diagnostics, scientific visualisation and StagLab 3.0. In: *Geosci. Model Dev.* 11 (6), S. 2541–2562. DOI: 10.5194/gmd-11-2541-2018.
Duretz, T., Petri, B., Mohn, G., Schmalholz, S. M., Schenker, F. L. & Müntener, O. (2016): The importance of structural softening for the evolution and architecture of passive margins. In: *Scientific reports* 6, S. 38704. DOI: 10.1038/srep38704.
Finger, N.-P., Kaban, M. K., Tesauro, M., Haeger, C., Mooney, W. D. & Thomas, M. (2021): A Thermo-Compositional Model of the Cratonic Lithosphere of South America Geochemistry, Geophysics, Geosystems. In: *Geochem. Geophys. Geosyst. DOI:* 10.1029/2020GC009307.
Geoffroy, L. (2005): Volcanic passive margins. In: *Comptes Rendus Geoscience* 337 (16), S. 1395–1408. DOI: 10.1016/j.crte.2005.10.006.
Granot, R. & Dyment, J. (2015): The Cretaceous opening of the South Atlantic Ocean. In: *Earth and Planetary Science Letters* 414, S. 156–163. DOI: 10.1016/j.epsl.2015.01.015.
Haas, P., Ebbing, J. & Szwillus, W. (2020): Sensitivity analysis of gravity gradient inversion of the Moho depth—a case example for the Amazonian Craton. In: *Geophysical Journal International* 221 (3), S. 1896–1912. DOI: 10.1093/gji/ggaa122.
Heine, C., Zoethout, J. & Müller, R. D. (2013): Kinematics of the South Atlantic rift. In: *Solid Earth* 4 (2), S. 215–253. DOI: 10.5194/se-4-215-2013.
Hunter, J. D. (2007): Matplotlib. A 2D Graphics Environment. In: *Comput. Sci. Eng.* 9 (3), S. 90–95. DOI: 10.1109/MCSE.2007.55.
Jarvis, G. T. & McKenzie, D. P. (1980): Sedimentary basin formation with finite extension rates. In: *Earth and Planetary Science Letters* 48 (1), S. 42–52. DOI: 10.1016/0012-821X(80)90168-5.
Johansson, L., Zahirovic, S. & Müller, R. D. (2018): The Interplay Between the Eruption and Weathering of Large Igneous Provinces and the Deep-Time Carbon Cycle. In: *Geophys. Res. Lett.* 45 (11), S. 5380–5389. DOI: 10.1029/2017GL076691.
Lister, G. S., Etheridge, M. A. & Symonds, P. A. (1986): Detachment faulting and the evolution of passive continental margins. In: *Geol* 14 (3), S. 246. DOI: 10.1130/0091-7613(1986)14<246:DFATEO>2.0.CO;2.

McDermott, C., Lonergan, L., Collier, J. S., McDermott, K. G. & Bellingham, P. (2018): Characterization of Seaward-Dipping Reflectors Along the South American Atlantic Margin and Implications for Continental Breakup. In: *Tectonics* 37 (9), S. 3303–3327. DOI: 10.1029/2017TC004923.

McKenzie, D. (1978): Some remarks on the development of sedimentary basins. In: *Earth and Planetary Science Letters* 40 (1), S. 25–32. DOI: 10.1016/0012-821X(78)90071-7.

Morgan, J. P., Taramón, J. M., Araujo, M., Hasenclever, J. & Perez-Gussinye, M. (2020): Causes and consequences of asymmetric lateral plume flow during South Atlantic rifting. In: *Proceedings of the National Academy of Sciences of the United States of America* 117 (45), S. 27877–27883. DOI: 10.1073/pnas.2012246117.

Moulin, M., Aslanian, D. & Unternehr, P. (2010): A new starting point for the South and Equatorial Atlantic Ocean. In: *Earth-Science Reviews* 98 (1-2), S. 1–37. DOI: 10.1016/j.earscirev.2009.08.001.

Müller, R. D., Cannon, J., Qin, X., Watson, R. J., Gurnis, M., Williams, S. et al. (2018): GPlates. Building a Virtual Earth Through Deep Time. In: *Geochem. Geophys. Geosyst.* 19 (7), S. 2243–2261. DOI: 10.1029/2018GC007584.

Müller, R. D., Zahirovic, S., Williams, S. E., Cannon, J., Seton, M., Bower, D. J. et al. (2019): A Global Plate Model Including Lithospheric Deformation Along Major Rifts and Orogens Since the Triassic. In: *Tectonics* 38 (6), S. 1884–1907. DOI: 10.1029/2018TC005462.

Mutter, J. C., Talwani, M. & Stoffa, P. L. (1982): Origin of seaward-dipping reflectors in oceanic crust off the Norwegian margin by “subaerial sea-floor spreading”. In: *Geol* 10 (7), S. 353. DOI: 10.1130/0091-7613(1982)10<353:OOSRIO>2.0.CO;2.

Nielsen, T. K. (2002): Formation of volcanic rifted margins. Are temperature anomalies required? In: *Geophys. Res. Lett.* 29 (21), S. 3623. DOI: 10.1029/2002GL015681.

Parsons, B. & Sclater, J. G. (1977): An analysis of the variation of ocean floor bathymetry and heat flow with age. In: *J. Geophys. Res.* 82 (5), S. 803–827. DOI: 10.1029/JB082i005p00803.

Pasyanos, M. E., Masters, T. G., Laske, G. & Ma, Z. (2014): LITHO1.0. An updated crust and lithospheric model of the Earth. In: *J. Geophys. Res. Solid Earth* 119 (3), S. 2153–2173. DOI: 10.1002/2013JB010626.

Rabinowitz, P. D. & LaBrecque, J. (1979): The Mesozoic South Atlantic Ocean and evolution of its continental margins. In: *J. Geophys. Res.* 84 (B11), S. 5973. DOI: 10.1029/JB084iB11p05973.

Renne, P. R., Ernesto, M., Pacca, I. G., Coe, R. S., Glen, J. M., Prévot, M. & Perrin, M. (1992): The age of parana flood volcanism, rifting of gondwanaland, and the jurassic-cretaceous boundary. In: *Science (New York, N.Y.)* 258 (5084), S. 975–979. DOI: 10.1126/science.258.5084.975.

Reston, T. J. (2009): The structure, evolution and symmetry of the magma-poor rifted margins of the North and Central Atlantic. A synthesis. In: *Tectonophysics* 468 (1-4), S. 6–27. DOI: 10.1016/j.tecto.2008.09.002.

Ringrose, P. S. & Meckel, T. A. (2019): Maturing global CO2 storage resources on offshore continental margins to achieve 2DS emissions reductions. In: *Scientific reports* 9 (1), S. 17944. DOI: 10.1038/s41598-019-54363-z.

Schaeffer, A. J. & Lebedev, S. (2013): Global shear speed structure of the upper mantle and transition zone. In: *Geophysical Journal International* 194 (1), S. 417–449. DOI: 10.1093/gji/ggt095.

Sengör, A. M. C. & Burke, K. (1978): Relative timing of rifting and volcanism on Earth and its tectonic implications. In: *Geophys. Res. Lett.* 5 (6), S. 419–421. DOI: 10.1029/GL005i006p00419.
Seton, M., Müller, R. D., Zahirovic, S., Williams, S., Wright, N. M., Cannon, J. et al. (2020): A Global Data Set of Present-Day Oceanic Crustal Age and Seafloor Spreading Parameters. In: *Geochem. Geophys. Geosyst.* 21 (10), S. 104508. DOI: 10.1029/2020GC009214.
Simon, K., Huismans, R. S. & Beaumont, C. (2009): Dynamical modelling of lithospheric extension and small-scale convection. Implications for magmatism during the formation of volcanic rifted margins. In: *Geophysical Journal International* 176 (1), S. 327–350. DOI: 10.1111/j.1365-246X.2008.03891.x.
Steinberger, B. & Becker, T. W. (2018): A comparison of lithospheric thickness models. In: *Tectonophysics* 746, S. 325–338. DOI: 10.1016/j.tecto.2016.08.001.
Thiede, D. S. & Vasconcelos, P. M. (2010): Paraná flood basalts. Rapid extrusion hypothesis confirmed by new 40Ar/39Ar results. In: *Geology* 38 (8), S. 747–750. DOI: 10.1130/G30919.1.
Thybo, H. & Artemieva, I. M. (2013): Moho and magmatic underplating in continental lithosphere. In: *Tectonophysics* 609, S. 605–619. DOI: 10.1016/j.tecto.2013.05.032.
Tugend, J., Gillard, M., Manatschal, G., Nirrengarten, M., Harkin, C., Epin, M.-E. et al. (2018): Reappraisal of the magma-rich versus magma-poor rifted margin archetypes. In: *Geological Society, London, Special Publications*, SP476.9. DOI: 10.1144/SP476.9.
Turcotte, D.; Schubert, G. (2018): Geodynamics: Cambridge University Press.
Wen, Z., Jiang, S., Song, C., Wang, Z. & He, Z. (2019): Basin evolution, configuration styles, and hydrocarbon accumulation of the South Atlantic conjugate margins. In: *Energy Exploration & Exploitation* 37 (3), S. 992–1008. DOI: 10.1177/0144598719840751.
Wernicke, B. (1981): Low-angle normal faults in the Basin and Range Province. Nappe tectonics in an extending orogen. In: *Nature* 291 (5817), S. 645–648. DOI: 10.1038/291645a0.
Zoback, M. L. & Mooney, W. D. (2010): Lithospheric Buoyancy and Continental Intraplate Stresses. In: *International Geology Review* 45 (2), S. 95–118. DOI: 10.2747/0020-6814.45.2.95.